Chapter 7

Effect of SiC on ablation mechanism and morphological evolution of in situ synthesized ZrB_2-SiC composites

7. 1 Introduction

In our present study, the synthesis of ZrB_2-SiC composites occurred by in-situ reduction of ZrO_2, B_4C, Si, and graphite (C) followed by hot pressing at 1500°C. The thermodynamic calculation revealed the feasibility of the reactions. SiC increased from 12 wt% to 30 wt% as the B_4C/Si and C/Si molar ratio decreased from 1.0 to 0.4 and 4.0 to 2.2, respectively. The hot-pressed ZrB_2-SiC composite was subjected to an oxy-acetylene flame to investigate the ablation and morphological evolution. The amount of SiC content depended on the molar ratio of B_4C/Si and C/Si. The microstructure of the ZrB_2-SiC composites before and after ablation was investigated. The thermal protection and ablation behavior of the ZrB_2-SiC composites strongly depended upon the material composition and processing parameters.

The primary objective of the present investigation was focused on the fabrication of ZrB_2-SiC composites via the in-situ reduction method at a lower synthesis temperature for TPS in ultra-high temperature applications. The detailed specification of the starting material has been explained in Chapter 4.

The reaction that occurs in the raw material is expressed as follows:

$$2ZrO_2\,(s) + B_4C\,(s) + Si\,(s) + 4C\,(s) \rightarrow 2ZrB_2\,(s) + SiC\,(s) + 4CO\,(g) \quad (7.1)$$

$$2ZrO_2\,(s) + B_4C\,(s) + 2Si\,(s) + 5C\,(s) \rightarrow 2ZrB_2\,(s) + 2SiC\,(s) + 4CO(g) \quad (7.2)$$

$$2ZrO_2\,(s) + B_4C\,(s) + 2.5Si\,(s) + 5.5C\,(s) \rightarrow 2ZrB_2\,(s) + 2.5SiC\,(s) + 4CO(g) \quad (7.3)$$

Table 7.1 The batch preparation of ZrO_2, B_4C, Si, and C for fabrication of ZrB_2-SiC composites

Sample name	Mol content				B_4C/Si	C/Si	Note
	ZrO_2	B_4C	Si	C			
ZSG1	2	1	1	4	1	4	Stoichiometric reaction (1)
ZSG2	2	1	2	5	0.5	2.5	1 mol addition of Si and C
ZSG3	2	1	2.5	5.5	0.4	2.2	1.5 mol addition of Si and C

After the fabrication of the samples, the present phase was investigated by an X-ray diffraction technique. The HR-SEM and EDS analysis revealed the microstructure and elemental analysis of the composite before and after the ablation test. The hot-pressed ZrB_2-SiC composites were subjected to oxy-acetylene flame to investigate the oxidation behavior at high temperatures up to 2600°C for 60 sec. The mass oxidation and linear ablation rates have been explained in chapter 4.

7. 2 Result and discussion

7.2.1 Thermodynamic calculation of ZrB_2-SiC composite

Thermodynamic calculations determine the feasibility of chemical reactions. For the chemical reactions, the free energy determines the standard Gibbs phase energy to produce energy at a given temperature. The feasibilities of the chemical reaction (7.1) are calculated by FACTSage thermochemical software [176], which is possible at 1324°C and under atmospheric pressure ($P=1.013*10^5$ Pa).

Similarly, reaction (7.2) and reaction (7.3) are feasible at 1229°C and 1171°C, respectively, lower than reaction (7.1). The Gibbs phase energy of chemical reaction (7.1), reaction (7.2), and chemical reaction (7.3) are negative at 1324°C, 1229°C, and 1171°C, respectively, and it reduces with an increase in processing temperature. Also, the amount of SiC content increases with decreasing the molar ratio B_4C/Si and C/Si.

7.2.2 Influence of temperature in different compositions

Fig. 7.1 shows the phase analysis of calcined ZSG1 at different temperatures. The minor amount of ZrB_2 (JCPDS card no 75-1050), SiC (JCPDS card no 29-1129), and silica (JCPDS card no 12-0251) phase detected at 1300°C with unreacted ZrO_2 and graphite (JCPDS card no 47-1155) phase. ZrB_2 and SiC powder form at 1300°C and above only. The temperature increased to 1400°C, and the residual silica reacted with graphite to form SiC. The ZrB_2 and SiC phase intensity increased with a minor amount of ZrO_2 and graphite in the powders. At 1500°C synthesis temperature, a significant amount of ZrB_2 and SiC powder was noticed through the XRD pattern, but still, a minor phase of ZrO_2 and graphite is present. It is hard to confirm that 1500°C is insufficient to transform graphite into SiC fully.

The ZrB_2 and SiC wt % are 75 % and 12 %, respectively, with the small amount of zirconia and graphite at 1500 °C analyzed by the Rietveld refinement method. Oxide impurity such as ZrO_2 at lower temperatures promotes coarsening of the grains, which limits the densification due to the formation of trapped porosity within the grains. The actual content of ZrB_2 and SiC is less, possibly due to intermediate borosilicate phase formation or the volatilization of Si in the form of a gaseous state during the process.

Various investigators have found that the 30 wt% of SiC provides high density [199], high strength [101], high hardness [109], high thermal conductivity [214], better ablation [174], thermal shock resistance [215] and oxidation resistance [160] as compared to single-phase ZrB_2. The advantage of SiC content for increasing mechanical qualities in ZrB_2-based ceramic is that the amount of SiC can be changed by varying the mole of the reactants [180].

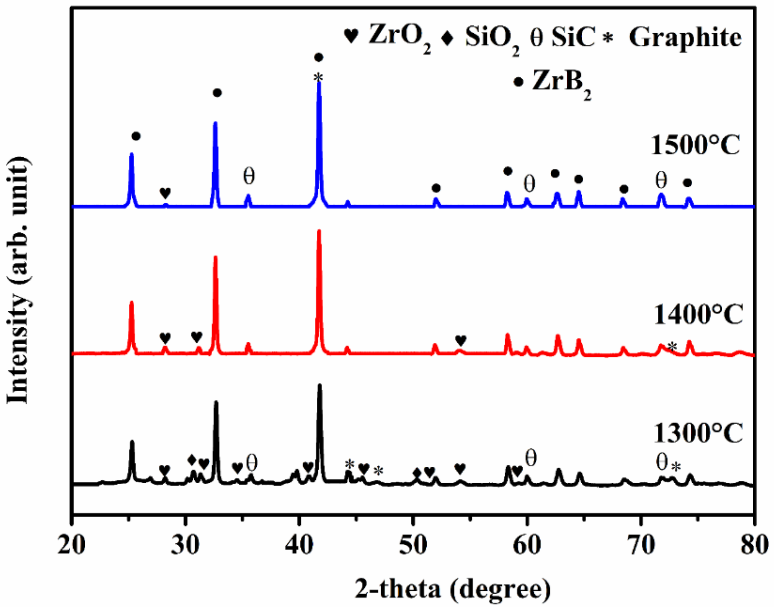

Fig. 7.1 XRD pattern of ZSG1 samples at a different processing temperature

7.2.3 Influence of molar ratio on optimization of SiC content in different compositions

Fig. 7.2 shows the phase analysis of ZSG1 to ZSG3 (various molar ratios) subjected to calcined at 1500°C. The XRD analysis revealed that when the molar composition of B_4C/Si and C/Si is 1 and 4, respectively, ZSG1 has 12 wt % SiC. As the molar ratio decreased to 0.5 and 2.5, the SiC content was 26.101 wt % with minor impurities. Further, the molar ratio reduces to 0.4 and 2.2 for B_4C/Si and C/Si, respectively. The amount of SiC is increased by 26 wt % to 30 wt %, which is helpful for oxidation resistance. The amount of ZrB_2 and SiC phase variation with the molar ratio is shown in Fig. 7.3.

The actual amount of the final product is always less than the calculated value. It may occur due to the intermediate B_2O_3 product formed during the boro/carbothermal reduction process. The intermediate B_2O_3 has been rapidly vaporized at high temperatures due to lower melting temperature (450°C) and higher vapor pressure [86], leading to the required extra amount of boron source for the complete conversion of ZSG3 composite. By varying the

reactant feed ratio, we can change the amount of ZrB_2, and SiC composition tends to enhance the oxidation resistance at higher temperatures [216].

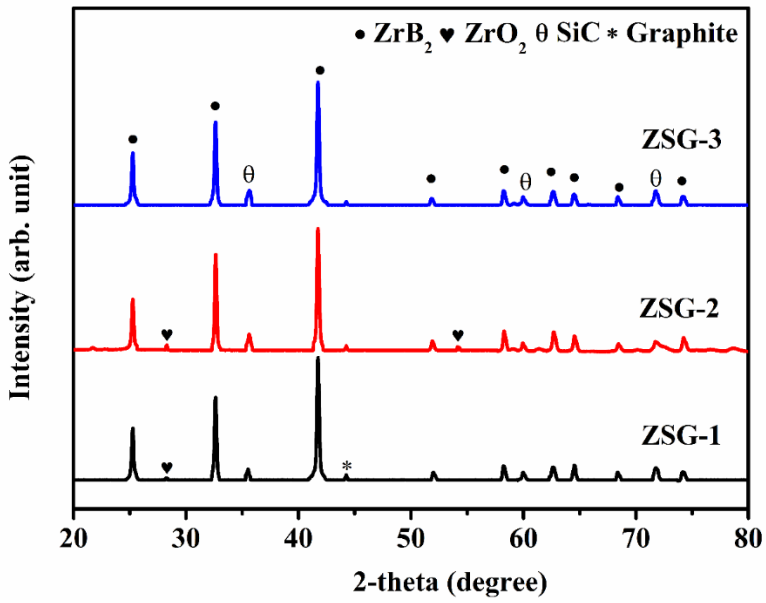

Fig. 7.2 XRD pattern of ZSG1 to ZSG3 (various molar ratios) at 1500°C

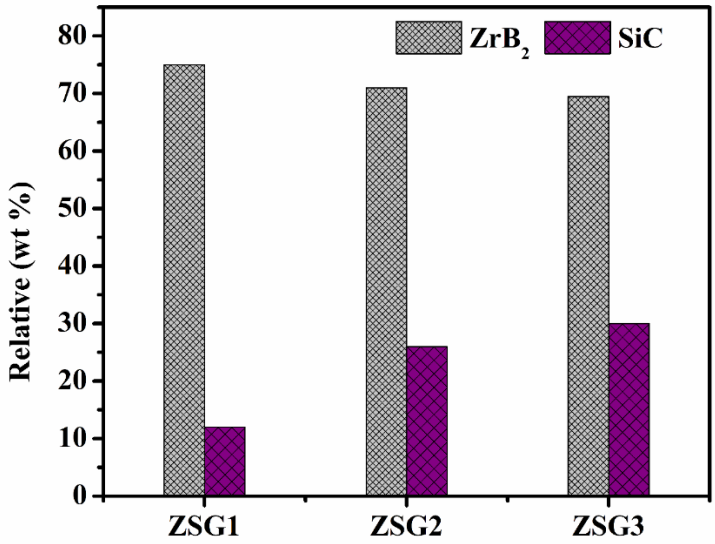

Fig. 7.3 The phase composition of ZSG1 to ZSG3 (various molar ratios) at 1500°C

7.2.4 Micrographs of synthesized ZrB_2-SiC powder

The morphology and microstructure of ZSG1 synthesized at 1500°C are displayed in Fig 7.4 (a-d). The HR-SEM image in Fig. 7.4 (a) illustrates the spherical granular, elongated

morphology and tiny particles formed during synthesis. The small particles are distributed in the ZrB_2-based composite. The aspect ratio of elongated shaped particles ranges from 2 to 3, with nearly circular diameters measuring 0.1 to 0.5 μm.

The EDS analysis employed the sample to determine the sample's elemental composition, as shown in Fig. 7.4 (b-d). Based on the EDS results, it is verified that the final composite contains Si, Zr, C, B, and O elements. The O was observed probably due to residual oxide impurities in the final composite. The EDS analysis at Points 1 and 3 primarily confirms the existence of Si and C elements. At Point 2, spherical particles are identified, comprising Si, Zr, C, and B elements.

The bond energy and inherent crystallographic properties are responsible for forming rod-shaped ZrB_2 structures. The high-energy plane grew faster than the other plane of ZrB_2 and finally disappeared, linked to the bond energies of the planes. The family of {110} plane with B-Zr bonds, growing faster and at the end disappearing, can be related to the energy distribution of Zr-Zr <B-Zr <B-B. Also, the slowest growth rate of the (001) plane with the Zr-Zr bond is responsible for the reserve in the structure. Apart from this factor, other factors contribute to the anisotropic development of ZrB_2. The molten B_2O_3 decreases the nucleation point at the intermediate synthesis stage, enhancing crystalline growth.

Furthermore, the constant supply of argon gas is causing the reduction of the supersaturation of B_2O_3, so the preferred development of ZrB_2 particles. The additional amount of SiC inhibited grain growth and restricted grain coarsening of the ceramics. Resultant single-phase ZrB_2 rod particles have a faster growth rate than ZrB_2-SiC composites.

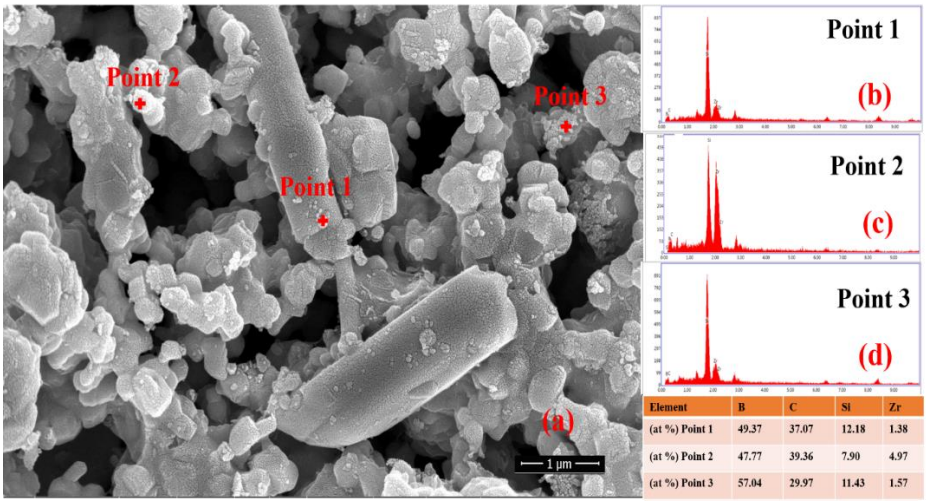

Fig. 7.4 (a) HR-SEM and (b)-(c) EDS of ZSG1 synthesized at 1500°C

The morphology and microstructure of the ZSG3 sample synthesized at 1500°C are displayed in Fig. 7.5 (a-d). Fig. 7.5 (a) shows that the average particle size of the ZSG3 sample is smaller than the ZSG1 sample due to the high amount of SiC contained in the composite, which acts as a grain growth inhibitor and hinders grain coarsening. In the HR-SEM image of the composite, numerous tiny particles are distributed in the large spherical granular particles. These tiny particles are responsible for decreasing the overall average particle size of the ZrB_2 composite. Fig. 7.5 (b) shows the high-magnification image of the small particle. The EDS compositions of Fig. 7.5 (a) and Fig. 7.5 (b) are illustrated in Fig. 7.5 (c) and Fig. 7.5 (d), respectively. In Fig. 7.5 (c), Zr, Si, C, and B are identified as the primary elements, while Fig. 7.5 (d) shows the predominant components of Si and C.

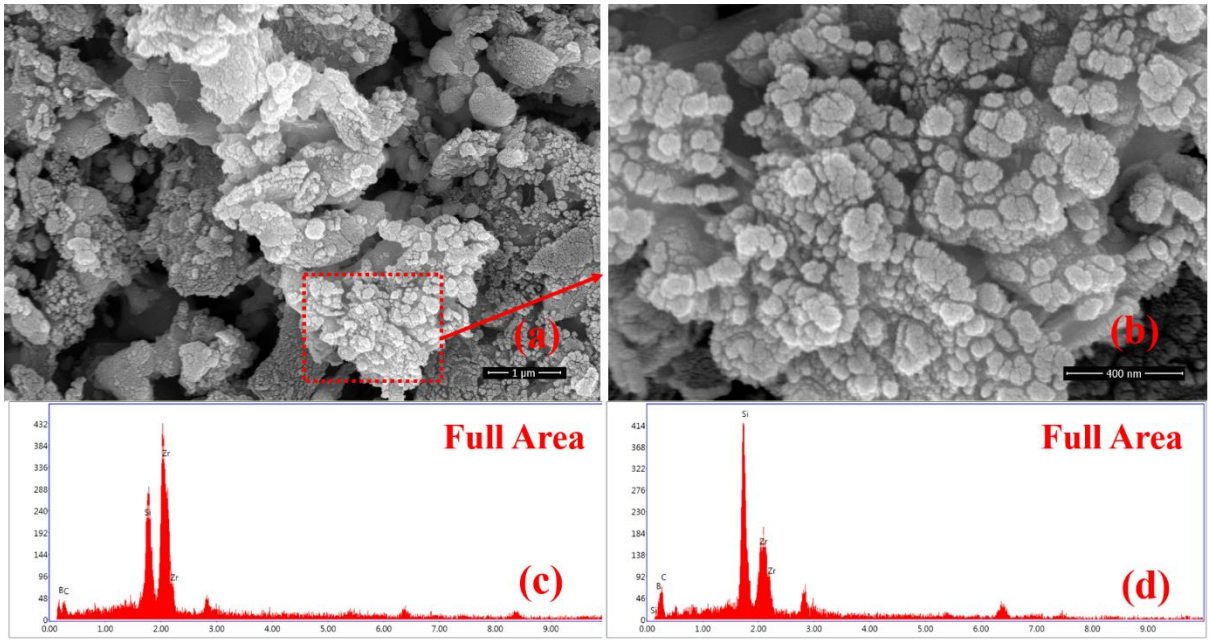

Fig. 7.5 (a), (b) HR-SEM and (c), (d) EDS of ZSG3 synthesized at 1500°C

The TEM image of ZSG3 powder is revealed in Fig. 7.6 (a)-(b). Fig. 7.6 (a) illustrates the particle size of ZSG3, which varied in the range of 200 nm-500 nm. Fig. 7.6 (b) shows the SEAD pattern of the junction of columnar and spherical particles, which consist of the (0001), $(10\bar{1}0)$, $(10\bar{1}1)$ and $(20\bar{2}0)$ crystal planes of ZrB_2 and (220) crystal planes of SiC. The TEM and SEAD results confirm the successfully synthesized ZrB_2 and SiC powder.

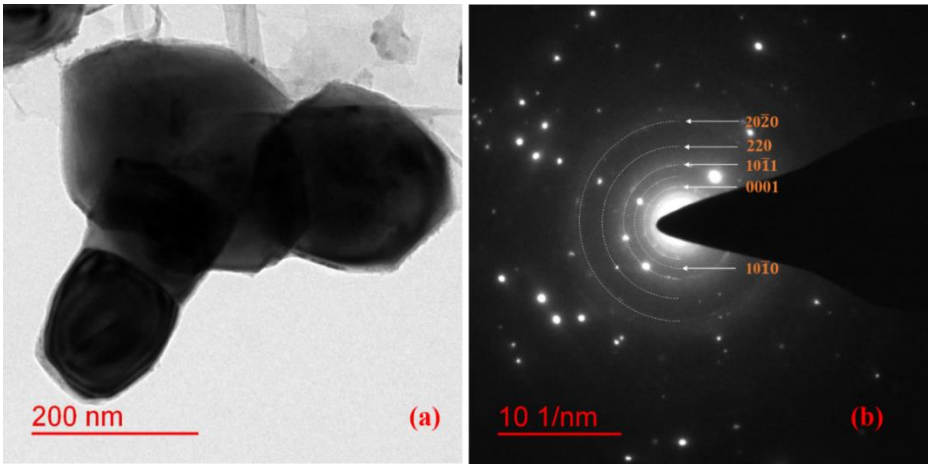

Fig. 7.6 TEM (b) SEAD pattern of ZSG3 synthesized at 1500°C

7.2.5 Micrographs of hot-pressed ZrB_2-SiC

The FESEM image of hot-pressed polished ZSG1 and ZSG3 samples was displayed in Fig.7.7 (a)-(b). Fig. 7.7 (a) revealed the microstructure of ZSG1, consisting of an irregular structure with more coarse particles. The high amount of porosity and coarse particles observed may be due to the presence of oxide particles, which hindered the densification phenomena during heat treatment. When the SiC content is optimized, the reduced particle size enhanced densification is confirmed in Fig. 7.7 (b). The hot-pressed ZrB_2-SiC composite (ZSG3) at 1500°C consists of a more homogeneous and densified microstructure verified through the polished micrograph. Fig. 7.7 (c) revealed the higher magnification graph of the polished surface. It consists of tiny particles along the grain boundary of ZrB_2. These SiC particles act as grain growth inhibitors to the samples. The increased SiC content is a grain growth inhibitor during the coarsening phenomenon. The driving force provides compaction during the heating of the samples. The hot-pressed ZSG1 and ZSG3 samples were characterized for the ablation test.

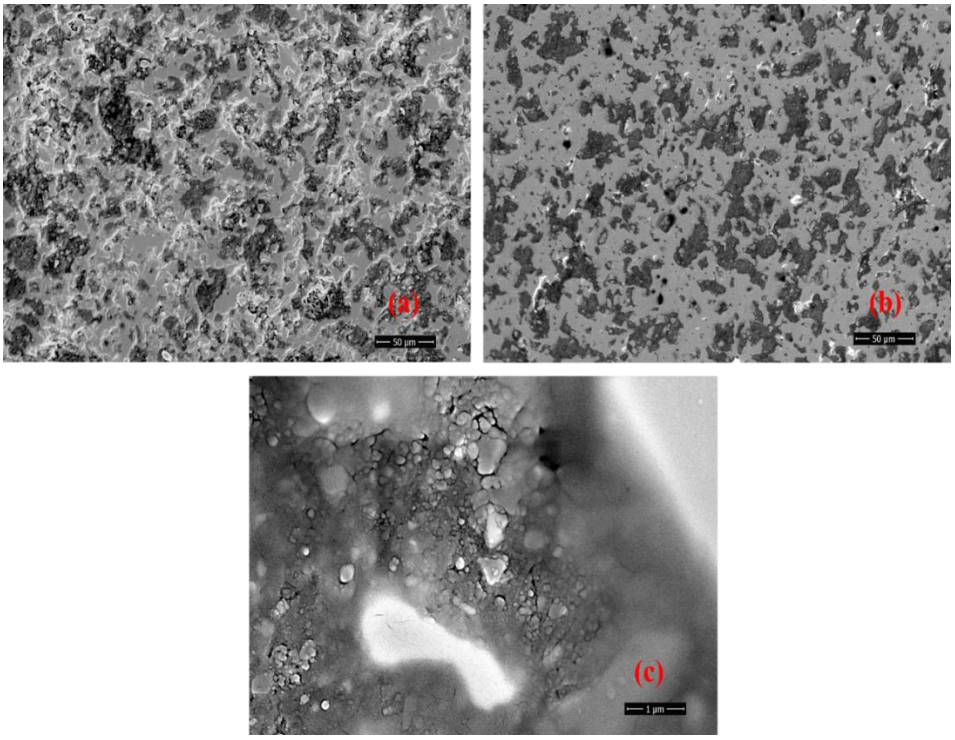

Fig. 7.7 HR-SEM of the hot-pressed surface of (a) ZSG1 and (b)ZSG3 (c) Higher magnification graph of ZSG3

7.2.6 Microstructure of ZrB_2-SiC composite after ablation

Fig 7.8 (a)-(b) shows the ablated surface of ZSG1 at 2600°C for 60 sec at various magnifications. Fig 7.8 (a) shows the irregular surface with elongated dendroid growth of particles. The formation of a dendroid structure may be due to irregular solidification of the sample during cooling. It consists of a micropore and crater on the surface due to gas overflow during ablation on the sample. The magnified surface morphology of the ZSG1 is illustrated in Fig 7.8 (d). The dendroid growth of the ZrO_2 particle occurs after fusion for a cooling duration of around 2500°C [217].

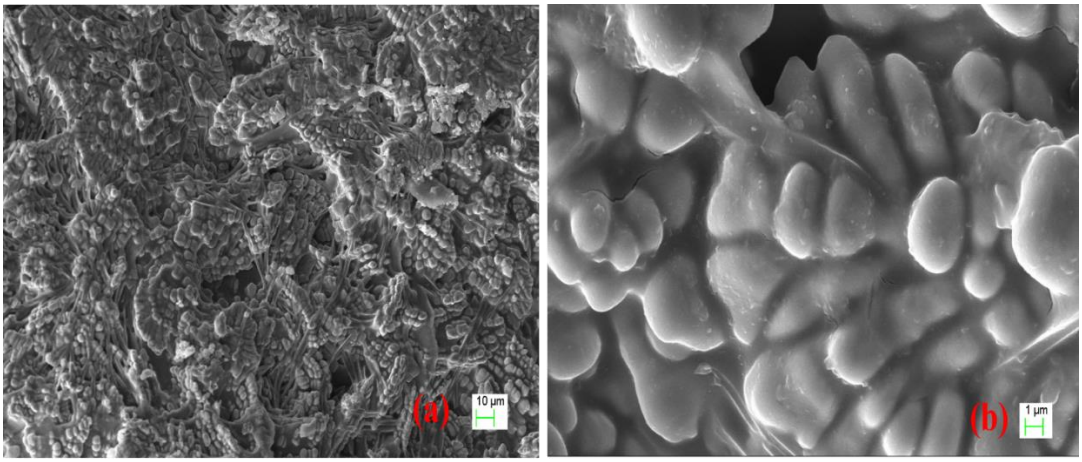

Fig. 7.8 (a)- (b) HR-SEM of oxidized surface of ZSG1 at 2600**°C** for 60 sec

Similarly, Fig. 7.9 (a)-(c) illustrates the morphology of the ablated surface of ZSG3 at 2600°C for 60 sec at various magnifications. In Fig. 7.9 (a), the surface of the ZrB_2-SiC composite consists of a melted structure with an irregular surface. The micrograph shows the presence of burst bubbles and craters of different depths on the dense oxide layer on the surface. These bubbles formed due to the escape of SiO_2 (g) (at around 1500°C) and other volatile products like CO (g) and B_2O_3(g) during the ablation process.

Fig. 7.9 (b) shows two types of oxide grains. The first is closely adherent equiaxed oxide grains, and the second is the elongated dendroid structured grains. Some relatively large grains can also be seen among equiaxed, finely dispersed grains due to the grain growth at a higher temperature. The elongated grains appeared to originate from particular nucleation sites and formed flowery structures. This is due to the thermal and compositional gradient on the topmost surface of the specimen, as the ablation temperature is high enough to convert ZrO_2 into a semi-solid (melting point of ZrO_2 (2680 °C)) state, but the time is not enough to melt the surface entirely.

Fig. 7.9 (c) shows the refined oxide grains dispersed in the molten scale of ZrO_2. This molten scale is formed most likely due to a heterogeneous mixture of ZrO_2 and SiO_2, which has a lower melting point than a single-phase ZrO_2 melting point (2680°C). Due to lack of time,

this molten phase comes out through pores and is deposited on the surface. The average grain size of oxide grains is 3µm. The sample ZSG1 consists of more irregular craters on the surface than the ZSG3 samples.

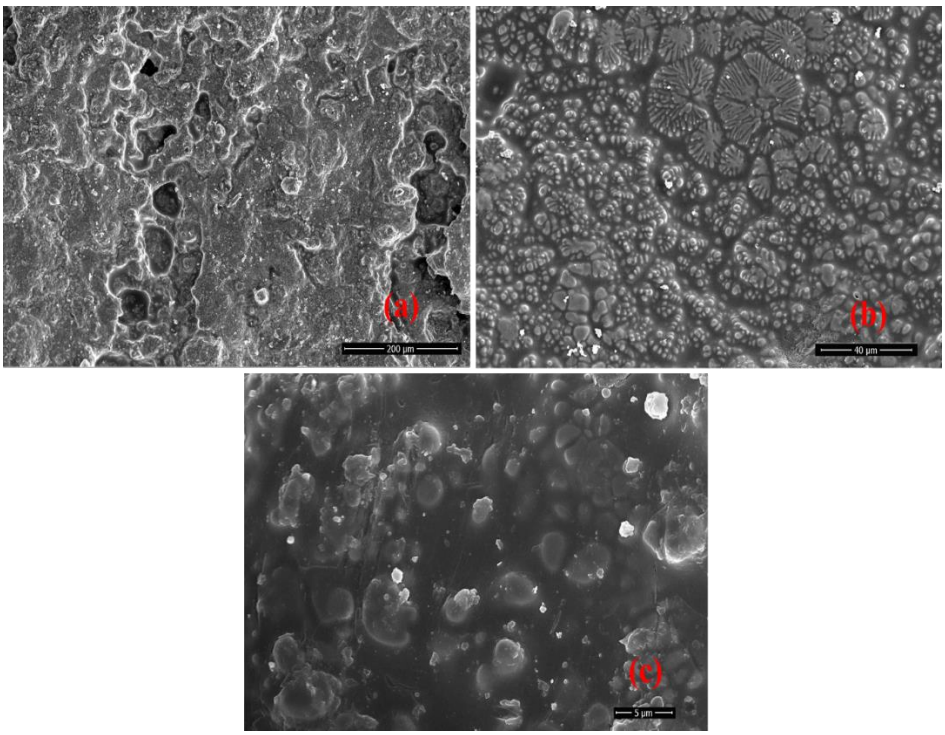

Fig. 7.9 (a) - (c) HR-SEM of oxidized surface of ZSG3 at 2600°*C* for 60 sec at various magnification

Fig. 7.10 (a) - (f) shows the HR-SEM and EDS spectra of the oxide scale on the fracture cross-section of ZSG1. The fracture cross-section of ZSG1 could be separated into three layers, as indicated by the red dotted line illustrated in Fig. 7.10 (a). The outermost layer has a delamination phenomenon due to the severe ablation of the surface. This layer mainly consists of melted bubbles and voids, formed primarily because of the advancement of the byproduct gases from the surface and lower layers during ablation. Beneath it, a porous layer formed due to high oxygen permeability through the outer surface. The increased oxygen permeability results in the slight delamination of the interlayer.

Fig. 7.10 (b) displayed the cross-section of the topmost layer, which has severe ablation compared to the inner layer. Fig. 7.10 (h) revealed the overall EDS spectrum of the top wall

mainly consists of Zr and O elements. Some Si elements and traces of boron and carbon elements are also present in this layer. The EDS analysis shows that the outer layer primarily consists of a ZrO_2 ceramic layer with some trapped SiO_2, which is visible in Fig. 7.10 (d). It can be observed that this layer primarily has ZrO_2 in bulk form (Point 3), but there are some places where higher content of Si and O and minor content of Zr (Point 1 & Point 2) were found in the spectrum, which indicates that some SiO_2 cannot escape during ablation and got trapped within ZrO_2 layer.

The outermost layer consists of a molten layer of ZrO_2 with a high no of pores attributed to the application temperature nearly equal to the melting point of ZrO_2, about 2680°C. It has been observed that the growth of the ZrO_2 particles is more evident than that of the ZrB_2 particles. Fig.7.10 (c) indicates the second interlayer's distinct dual structures of particles. Compared to the outermost/topmost layer, this layer has a comparatively high amount of SiO_2. Flake-shaped SiO_2 particles occur in between the molten ZrO_2. From the above observation, the three layers of oxides are present on the surface. The outermost layer is attributed to the ZrO_2 layer (average thickness 450 μm), the second layer is related to the SiO_2 dense/rich layer (average thickness 350 μm), and the third porous layer is the SiC-depleted layer.

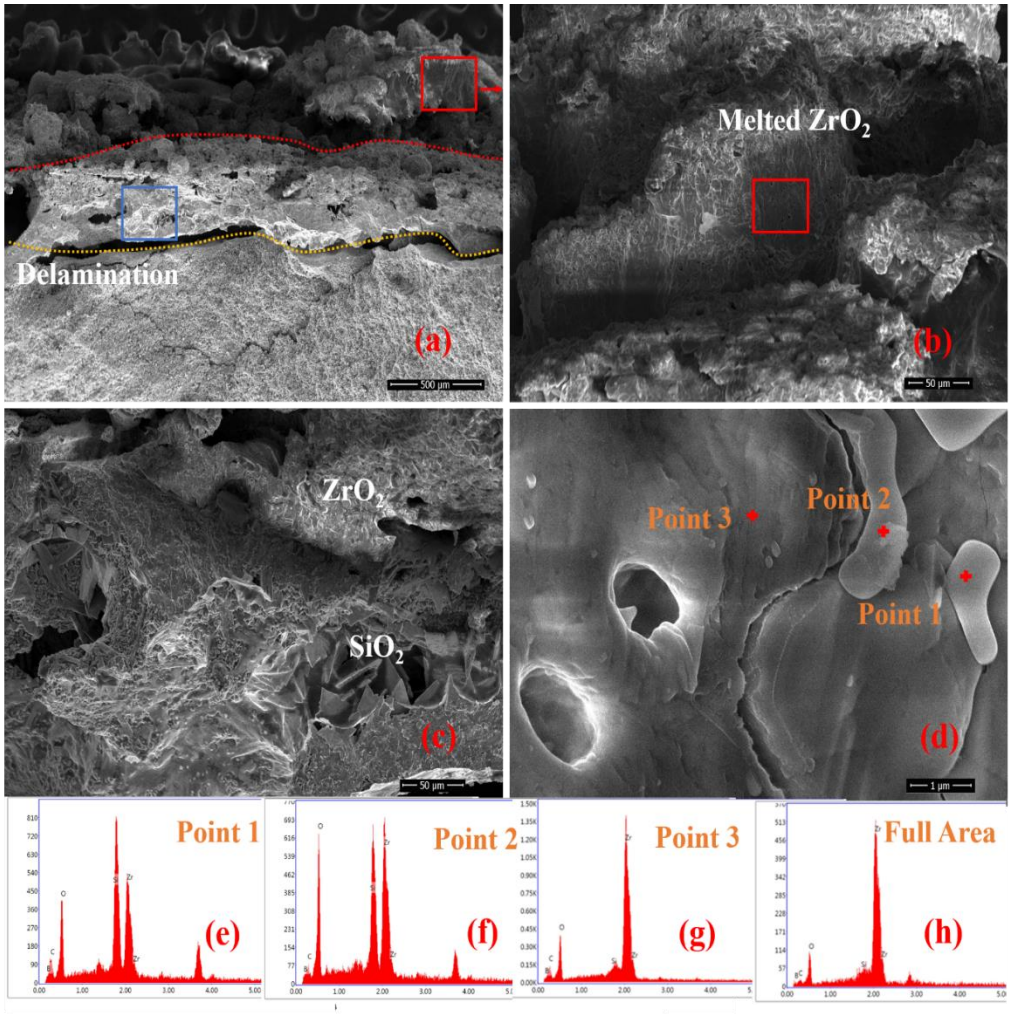

Fig. 7.10 (a)-(h) HR-SEM and EDS of the oxidized fractured cross-section of ZSG1 at 2600°C for 60 sec

Fig. 7.11 (a)-(h) shows the microstructure and EDS spectra of the fracture cross-section of ZSG3 samples after the ablation test on the sample surface at 2600°C for 60 sec. In Fig. 7.11 (a), three distinct layers can be observed without delamination or peeling in the HR-SEM image. Strong adhesion and bonding between the outermost and interface layers are responsible for the delamination-free samples. The ablation of ZSG3 samples was inferior to the ZSG1 samples. Also, the morphology and microstructure of the layers were slightly different.

As the SiC content in the ZrB_2-SiC composite increases, a higher amount of SiC is transformed into the SiO_2 phase during the ablation test. The SiO_2 phase diffuses to the outer surface by losing some energy during the evaporation process. It happened due to smaller ZrO_2

particles with larger pores forming in the ZSG3 samples than in the ZSG1 samples. The thickness of the ZrO_2 layer of ZSG3 is smaller than that of the ZSG1 samples.

A ZrO_2 porous layer on the outermost surface in Fig. 7.11 (a) confirms the escaping of gaseous products from the oxidation of ZrB_2 and SiC. Beneath the outermost ZrO_2 layer, a continuous molten layer with several bubbles was observed in Fig 7.11 (b), which was confirmed as Si and O element (point 4) by EDS elemental analysis in Fig. 7.11 (e). The low oxygen permeability of the SiO_2 layer prevents the interface layer from oxidation and high ablation temperature. Fig. 7.11 (c) shows a closer look at the red spherical area from Fig. 7.12 (b). It consists of the well-growth and minimal-grow fibrous structure indicated by points 5 and 6, respectively, identified as Si and O elements from the EDS analysis shown in Figures 7.11 (f) and 7.11 (g). The well-developed fibrous SiO_2 structure on the surface of large particles can be correlated with the oxidation of SiC particles. These SiC particles were distributed on the large spherical ZrB_2 particles, as mentioned in Fig. 7.6. The minor growth in fibrous structure occurred due to insufficient temperature reaching the surface. Fig. 7.11 (d) shows a porous microstructure under this layer. The EDS analysis of this layer, in Fig. 7.11 (h), confirms this layer belongs to the SiC depletion layer because it primarily Zr and B signals with minor signals of the C element beneath the oxide-containing layers. The depletion of SiC content causes the porosity in this layer. The upper portion of the depletion layer displays a small amount of SiO_2 beneath the depletion layer/ZrO_2 interface, demonstrating the oxidation of the SiO (g) to SiO_2 happens near the ZrB_2/ZrO_2 interface. The weak C signal in EDS shows the partial depletion of SiC, which can be related to the moderately disbursed SiC grains during rapid ablation. The outermost oxide thickness of ZrO_2, subsequently SiO_2 and SiC depleted layer is 330 μm, 120 μm, and 450 μm, respectively.

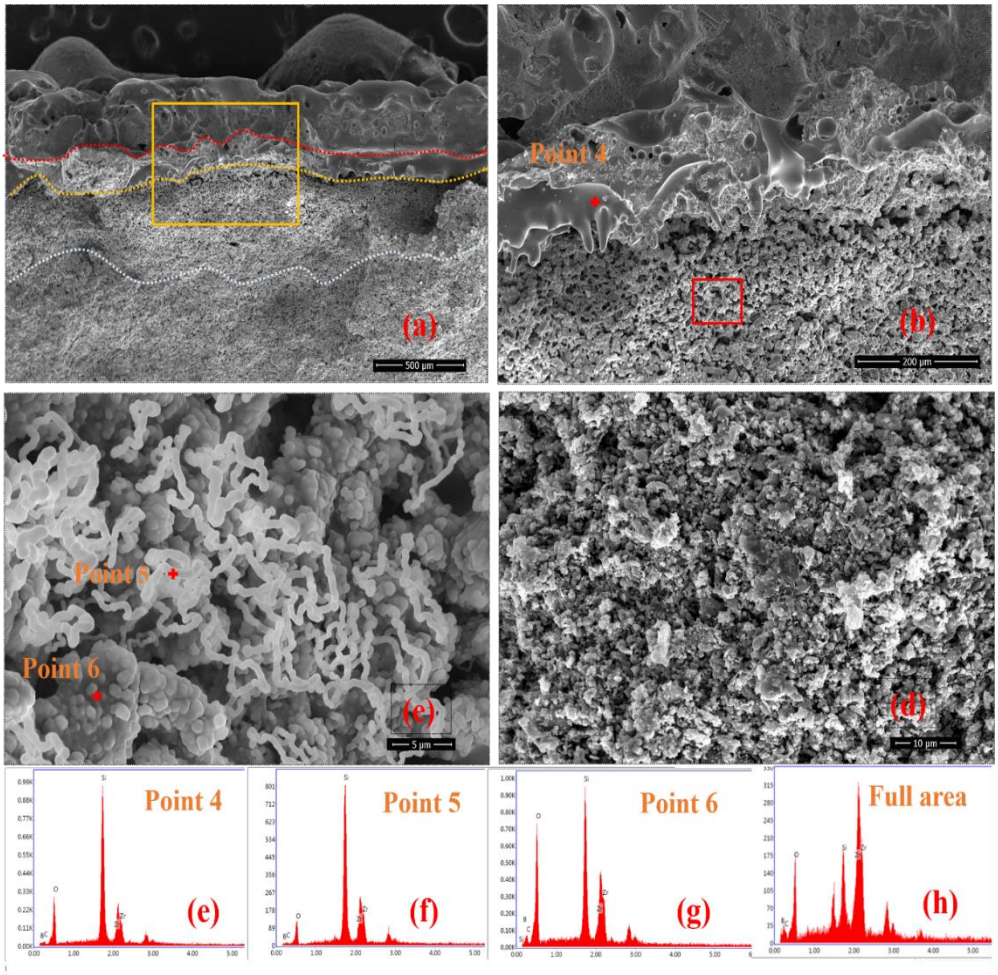

Fig. 7.11 (a)-(f) HR-SEM and EDS of the oxidized fractured cross-section of ZSG 3 at 2600 °C for 60 sec

7.2.7 Ablation rate of ZrB_2-SiC composite

The linear and mass ablation rates of the ZSG1 and ZSG3 are mentioned in Table 7.2. After ablation, the thickness of the samples was increased from 6 mm to 8.04 mm and 5.8 mm to 6.1 mm for ZSG1 and ZSG3, respectively. The linear ablation rates of ZSG1 and ZSG3 are -3.4 µm/s and -0.35 µm/s, respectively. The negative value of the linear ablation rate indicated the increasing thickness of the ZrB_2-SiC composite during ablation due to the formation of an oxide layer on the surface. When the SiC content in the ZSG3 sample increases, the linear ablation rate decreases compared to ZSG1.

During the heating condition of ZrB_2-SiC composite, SiC plays an essential role in providing thermal protection by the formation of a SiO_2 layer on the surface by the oxidation of SiC to protect the beneath layer of composite as shown in Fig 7.10 and Fig. 7.11. The SiO_2 and B_2O_3 evaporates rapidly, only the skeleton structure of ZrO_2 occurs on the outermost layer, which is very crucial for dimensional stability. A higher amount of SiC content led to more mass loss of the ZrB_2-SiC composite. The mass loss of the ZSG1 and ZSG3 is 0.380 mg/s and 0.852 mg/s, respectively. The mass ablation rate of ZSG1 is nearly half of the ZSG3 sample. The linear and mass ablation rates of the ZrB_2-SiC composites shown in Table 7.2.

Table 7.2 Mass and linear ablation rate of the ZrB_2-SiC composites

Final Composite	Thickness of sample (mm)		Oxide layer thickness (μm)	Mass loss rate (mg/s)	Linear ablation rate μm/s
	Before ablation	After ablation			
ZrB_2-12 % SiC	6	8.04	900	0.380	-3.4
ZrB_2-30 % SiC	5.8	6.01	950	0.852	-0.35

7.2.8 Ablation mechanism

During the ablation test, the surface oxidation of the composite occurred. As time passes, the thickness of the oxide layer increases due to increasing the oxidation product. If the product formed during oxidation has a lower melting point than the applied temperature, the oxide product will evaporate, and mass losses will occur. Therefore, more mass losses and high oxide layer thickness are associated. The behavior of this refractory oxide influences the linear ablation rate.

The oxide layer thickness of ZSG3 is about 950 μm (Fig. 7.11) higher than the ZSG1, about 900 μm (Fig. 7.10), and the mass ablation rate of ZSG3 is 0.852 mg/s higher than the ZSG1, about 0.380 mg/cm^2 s. The oxide products occur in ZSG1 and ZSG3 samples. Among all oxide products, ZrO_2 has the highest melting point. As a result, the behavior of ZrO_2 is the deciding factor for the linear ablation rate instead of oxide layer thickness.

In the ablation procedure, upon the application of the flame on the surface, the temperature reached nearly 2600°C, and the ZrB_2-SiC composite started to oxidize rapidly into ZrO_2, SiO_2, CO, and B_2O_3 according to reactions (7.4) and (7.5). Except for ZrO_2, other oxides such as CO, B_2O_3, and SiO_2 were quickly evaporated at this high temperature. Thus, the outermost surface of the ZrO_2 skeleton layer had increased pores.

$$ZrB_2\,(s) + 2.5O_2\,(g) \rightarrow ZrO_2\,(l) + B_2O_3\,(g) \quad (7.4)$$

$$SiC\,(s) + 2O_2\,(g) \rightarrow SiO_2\,(g) + CO_2\,(g) \quad (7.5)$$

Beneath it, due to the lower temperature, the evaporation rate of B_2O_3 and SiO_2 is slightly lower than that of the uppermost surface. Relatively, B_2O_3 and SiO_2 have a lower saturation vapor pressure. Therefore, it fills the ZrO_2 skeleton's pores to form a homogeneous SiO_2 dense layer, according to reactions (7.6) and (7.7). This continuous SiO_2 thick layer reduces the oxygen permeability and minimizes oxygen diffusion, named the oxidation resistance layer [216].

$$ZrB_2(s) + 2.5O_2\,(g) \rightarrow ZrO_2\,(s) + B_2O_3\,(g) \quad (7.6)$$

$$SiC\,(s) + 2O_2\,(g) \rightarrow SiO_2\,(l) + CO_2\,(g) \quad (7.7)$$

As the ablation process continues, active oxidation of the SiC depletion layer is observed in unoxidized ceramic due to the inward transportation of oxygen through the SiO_2-dense/rich layer. The active oxidation of SiC is responsible for forming SiO and CO products mentioned in the reaction (7.8). These oxides, like SiO and CO, react with oxygen converted into SiO_2 and CO_2, respectively (reactions 7.9 and 7.10). This liquid SiO_2 was converted into gaseous SiO_2 and combined with CO_2 to form bubbles in the dense SiO_2 layer.

In the SiC-depleted region, oxygen pressure is far lower than other oxide layers, forming a porous SiC depletion layer with limited oxidation of ZrB_2. Under these oxides' layers and depletion layer, the ZrB_2-SiC composite consists of a minor amount of ZrO_2 as base material. Fig 7.12 illustrates the ablation process for the TPS.

$$SiC(s) + 0.5O_2(g) \rightarrow SiO(g) + CO(g) \quad (7.8)$$

$$SiO(g) + O_2(g) \rightarrow SiO_2(l) \quad (7.9)$$

$$CO(g) + O_2(g) \rightarrow CO_2(g) \quad (7.10)$$

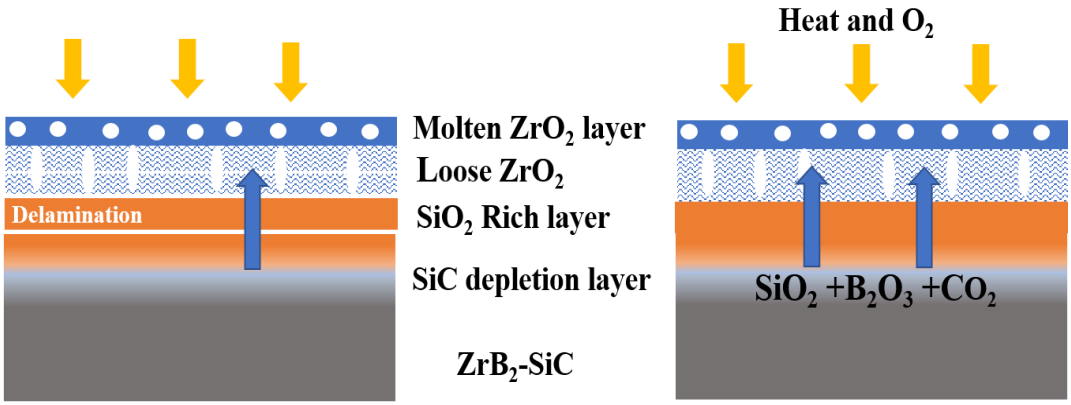

Fig. 7.12 Schematic representation of oxide layer during ablation of ZrB_2-SiC composite

7. 3 Conclusion/ Summary of the chapter

This study successfully established the synthesis of ZrB_2-SiC composites via the in-situ reduction method at low temperatures using ZrO_2, B_4C, Si, and graphite as raw materials. The synthesized fine ZrB_2-SiC powder was subsequently hot pressed at 1500°C. The ZSG1 composite had only 12 wt % of SiC in the ZrB_2-SiC composite, which is insufficient to provide oxidation and ablation resistance at 2600°C. So, the molar ratio of B_4C/Si and Si/C decreased from 1 to 0.4 and 4 to 2.2, respectively, increasing SiC from 12 wt% to 30 wt%. Homogeneously distributed 30 wt% SiC particles restrict the grain growth of the ZrB_2 particles. The micrographs confirm that a higher amount of the SiC (ZSG3) provides better dimensional

stability during ablation than 12 wt % of SiC content (ZSG1). During the ablation test, oxidation of composites and evaporation of oxides are responsible for forming the ZrO_2 layer, SiO_2 dense layer, and SiC depletion layer. During ablation, which occurs at 2600°C, a continuous thick SiO_2 layer forms beneath the ZrO_2 layer. This SiO_2-dense layer has a low diffusion coefficient of oxygen, which is responsible for developing the SiC-depleted layer by the active oxidation of SiC. Therefore, the above study proves that the fabrication of the in situ synthesized ZrB_2-SiC composites was successful at low processing temperatures via hot pressing for ultra-high temperature applications.